This is the author's version of an article that has been published in this journal. Changes were made to this version by the publisher prior to publication.
The final version of record is available at http://dx.doi.org/10.1109/JLT.2018.2834153

Passive Opto-Antenna as Downlink Remote Antenna Unit for Radio Frequency over Fiber

Olivier Caytan[1], *Student Member, IEEE,* Laurens Bogaert[1,2], Haolin Li[1], *Student Member, IEEE,* Joris Van Kerrebrouck[1], *Student Member, IEEE,* Sam Lemey[1], *Member, IEEE,* Guy Torfs[1], *Member, IEEE,* Johan Bauwelinck[1], *Member, IEEE,* Piet Demeester[1], *Fellow, IEEE,* Sam Agneessens[1], *Member, IEEE,* Dries Vande Ginste[1], *Senior Member, IEEE,* and Hendrik Rogier[1], *Senior Member, IEEE*

***Abstract*—A novel remote antenna unit, intended for application in the downlink of an analog radio frequency over fiber system, is proposed, whose radiated power originates entirely from the optical signal supplied by a single multi-mode fiber. By operating the photodetector of the optical receiver at zero bias voltage, while omitting typical active components, such as transimpedance amplifiers, a fully passive unit, requiring no external power supply, is obtained. Instead, a careful co-design is performed to maximize the power transfer from photodetector to antenna within the frequency range of interest using an impedance matching network. A wideband cavity-backed slot antenna is implemented in air-filled substrate-integrated-waveguide technology. The antenna feed plane serves as integration platform for the optical receiver. The resulting downlink remote antenna unit is compact, cost-effective, energy-efficient and extremely reliable. Therefore, it is an ideal building block for novel, highly specialized, ultra-high density wireless communication systems, which require massive amounts of remote antenna units, deployed in attocells as small as $15\,\mathrm{cm} \times 15\,\mathrm{cm}$. A prototype operating in a wide frequency bandwidth ranging from $3.30\,\mathrm{GHz}$ to $3.70\,\mathrm{GHz}$ is constructed and validated. In free-space conditions, a broadside gain of $-0.2\,\mathrm{dBi}$, a front-to-back ratio of $8.8\,\mathrm{dB}$ and linear polarization with a cross-polarization level of $-28.8\,\mathrm{dB}$ are measured at $3.50\,\mathrm{GHz}$. Furthermore, a $-3\,\mathrm{dB}$ gain bandwidth of $500\,\mathrm{MHz}$ is observed. Finally, the prototype is deployed in a unidirectional data link, achieving a symbol rate of $80\,\mathrm{MBd}$ over a distance of $20\,\mathrm{cm}$.**

***Index Terms*—Air-Filled Substrate-Integrated-Waveguide (AF-SIW) Cavity-Backed Slot Antenna, Attocells, Citizens Broadband Radio Service (CBRS), Downlink Remote Antenna Unit (DL-RAU), Matching Network, Opto-Antenna, Radio Frequency over Fiber (RFoF).**

I. Introduction

Radio over fiber (RoF) architectures [1], [2] exploit the advantages of optical fiber, which include low attenuation, high bandwidth and immunity against electromagnetic interference (EMI), for the transmission of radio signals. Furthermore, RoF architectures provide reduced complexity, especially when applying analog radio frequency over fiber (RFoF). In RFoF systems, the radio frequency (RF) signals are immediately modulated onto the optical carrier. Thereby, the remote antenna units (RAUs) only need to implement amplification and conversion between the optical and electrical domains, while frequency translation is entirely avoided. This enables centralization of the most expensive equipment, such as the RF transceivers, at a central office (CO), leading to a very flexible system with low complexity. As such, RFoF is a key technology for novel, highly specialized, ultra-high density wireless communication systems as proposed in [3], [4]. These systems target futuristic application scenarios different from the ones conventionally considered in 5G, such as factory-of-the-future environments that are densely populated by numerous autonomous robots. Such wireless communication scenarios are characterized by a very high density of mobile users, demanding a high bandwidth wireless connection, with low latency and high reliability. To achieve the extremely high bit rate density, massive amounts of RAUs are deployed, which are integrated into the floor and operate in ultra-small attocells as small as $15\,\mathrm{cm} \times 15\,\mathrm{cm}$. In addition, the use of millimeter-wave (mmWave) frequencies is foreseen to accommodate the high bandwidths and to reduce interference between adjacent cells. Due to their massive amount, the RAUs need to be extremely low cost and low power to make this solution cost-effective.

This paper concentrates on the downlink (DL) subsystem of the RFoF architecture, which implements the wireless transmission of the RF signals sent to the RAU. It describes the design and validation of a novel, fully passive downlink RAU (DL-RAU) intended for an ultra-high density wireless communication system as proposed in [3]. Full passivity implies photodetectors operating at zero bias voltage ($0\,\mathrm{V}$), as well as omitting other active components such as transimpedance amplifiers (TIAs). This means that the DL-RAU is entirely driven by optical power, leading to a maintenance-free and cost-effective unit. Cost-effectiveness is further enhanced by operating at an optical wavelength of $0.85\,\mu\mathrm{m}$, using multi-mode fiber, and adopting vertical-cavity surface-emitting lasers (VCSELs) with a direct modulation scheme [5], which is justified when assuming that the propagation distance in the optical interconnection network serving the attocells is sufficiently short. To achieve this goal, the optoelectronic circuitry and the antenna are carefully co-designed with a band-pass impedance matching network to extract as much RF power as possible from the photodetector within a specified bandwidth of operation. Specifically, the DL-RAU covers the frequency range from $3.30\,\mathrm{GHz}$ to $3.70\,\mathrm{GHz}$, which includes the Citizens Broadband Radio Service ($3.55\,\mathrm{GHz}$ – $3.70\,\mathrm{GHz}$)

[1] Ghent University - imec, IDLab, Department of Information Technology (Olivier.Caytan@UGent.be).
[2] Ghent University - imec, Photonics Research Group, Department of Information Technology.

Copyright (c) 2018 IEEE. Personal use of this material is permitted. However, permission to use this material for any other purposes must be obtained from the IEEE by sending a request to pubs-permissions@ieee.org.

Copyright (c) 2018 IEEE. Personal use is permitted. For any other purposes, permission must be obtained from the IEEE by emailing pubs-permissions@ieee.org.

This is the author's version of an article that has been published in this journal. Changes were made to this version by the publisher prior to publication.
The final version of record is available at http://dx.doi.org/10.1109/JLT.2018.2834153

[6], as a demonstration of the concept at lower frequencies. It is important to note that the impedance matching technique, which optimizes the performance in a specified frequency band, can be applied without major modifications to biased photodetectors operating at longer wavelengths using single-mode fiber. By means of an optical amplifier, higher transmit powers can be achieved. While this would negate passivity, it would result in a more versatile DL-RAU that is able to operate in larger cells, including conventional 5G application scenarios.

The antenna is implemented in air-filled substrate-integrated-waveguide (AFSIW) technology [7], where a waveguide structure, geometrically identical to a conventional rectangular metallic waveguide filled with air, is integrated into a multi-layer printed circuit board (PCB). The technology relies on milling a rectangular cavity in a substrate with two conducting layers and subsequently metallizing the sidewalls of this cavity through edge-plating. The waveguide is formed by covering the edge-plated cavity on both sides with a conducting layer to form the top and bottom walls. Accurate alignment is ensured by using alignment holes, while electrical contact is achieved by soldering [7] or tightening alignment pins [8]. Transitions from other waveguides, such as microstrip, toward AFSIWs have been reported [7], [9]. Furthermore, several devices originally implemented in rectangular waveguide were realized in AFSIW technology, including filters [7], phase shifters [10], and antennas [8], [11]. These AFSIW implementations preserve the benefits of a rectangular waveguide, in particular its low propagation loss, high quality factor, and high electrical shielding between different devices. Moreover, they remain fully compatible with standard PCB fabrication processes. The AFSIW cavity-backed slot antenna topology proposed in [8] is adopted, which relies on a rectangular aperture in the bottom or top conducting wall for radiation. Its low profile and planar structure enable a close integration with the optoelectronic circuitry, while preserving a high isolation between both.

Several energy-autonomous RAUs that rely on power over fiber (PoF) to feed all active electronics have been proposed in literature [12]–[19]. At first, separate optical fibers were used for transmission of the optical power and the RF signal [12]–[14]. Later on, the optical power and the RF signal were carried simultaneously by a single optical fiber, by applying wavelength division multiplexing (WDM) [15], [16], or by using double-clad fibers (DCFs) [17]–[19], consisting of a single-mode core and a multi-mode inner cladding. By contrast, in this paper, full energy-autonomy is achieved in a DL-RAU by omitting all active components and maximizing power transfer from photodetector to antenna by means of a passive impedance matching network, in the meantime enhancing cost-effectiveness. In [20], a fully passive mmWave radio transmitter powered by a single optical fiber was proposed, employing a photodetector specifically designed for zero bias operation. However, no impedance matching network was used to increase the radiated RF power. Several other antennas integrated with photodetectors have already been reported in literature [21]–[32]. In [21] and [22], planar mmWave antennas with integrated photodiode are proposed, operating at 60 GHz and 120 GHz, respectively. Furthermore, in [23]–[26], ultra-wideband (UWB) tightly coupled arrays have been proposed, in which the elements are fed by photodetectors. In most cases, high-power modified uni-traveling carrier (MUTC) photodiodes are applied to achieve a high radiated power, rendering electrical amplifiers unnecessary. Alternative UWB antenna topologies have also been proposed, including connected arrays [27]–[30], aperture-coupled patch antennas [31], and patch antenna arrays [32]. Owing to the extent of the achieved frequency bandwidth, multiple functionalities can be served by the same antenna aperture. However, most applications require coverage of a specific frequency band, and applying the proposed UWB antenna topologies for these applications will result in a sub-optimal power efficiency. Indeed, as a result of the Bode-Fano criterion [33]–[35], any efficient power transfer from photodetector to antenna in a frequency band that is left unused, will degrade the achievable power transfer in the useful frequency range. By applying impedance matching networks, the power transfer is optimized in the specified frequency band only. Broadband impedance matching of a high-speed photodetector using a low-pass matching network was first proposed in [36] to improve optical receiver sensitivity. However, the resulting matching network was not entirely lossless, as matching resistors were used. To the best of the authors' knowledge, this paper presents the first fully passive DL-RAU, which operates in a specified frequency bandwidth by virtue of a practically lossless band-pass impedance matching network, and requires no bias voltage.

Section II discusses all design aspects of the passive DL-RAU. Details are provided about the employed photodetector, the antenna structure and the co-design technique adopted to achieve impedance matching between these components. In Section III, the developed DL-RAU is validated through measurements on a constructed prototype. The conclusion and an outlook for further research are provided in Section IV.

II. Passive Downlink Remote Antenna Unit Design

A. RFoF Scheme and DL-RAU Co-Design Strategy

Fig. 1a displays a high-level schematic overview of the adopted analog RFoF scheme and the proposed DL-RAU. A VCSEL is biased with a current I_B, generating a quiescent optical power P_B. Furthermore, the VCSEL's current is directly modulated by an RF signal source, such that its output is intensity modulated. The RF signal is intended for wireless transmission and its power is contained within a bandwidth ranging from 3.30 GHz to 3.70 GHz. The RF signal's peak power should remain sufficiently low in order to avoid distortion by the VCSEL [37]. A bias tee, represented by an ideal RF choke and DC block capacitor in Fig. 1a, combines the RF signal and bias currents. A multi-mode fiber guides the generated optical power towards the DL-RAU. A short optical link is assumed, such that propagation loss and dispersion can be neglected. The DL-RAU consists of two tightly integrated subsystems, being the optoelectronic conversion circuit and the antenna. The key component in the optoelectronic conversion circuit is the PIN photodetector,

Copyright (c) 2018 IEEE. Personal use is permitted. For any other purposes, permission must be obtained from the IEEE by emailing pubs-permissions@ieee.org.

This is the author's version of an article that has been published in this journal. Changes were made to this version by the publisher prior to publication.
The final version of record is available at http://dx.doi.org/10.1109/JLT.2018.2834153

whose active region is illuminated by the optical fiber. As a result, the DL-RAU's photodetector generates a photocurrent that is proportional to the received optical power with responsivity R expressed in units of $\mathrm{A\,W^{-1}}$ [5], and consists of a direct current (DC), which originates from the average optical power, and a time-varying current, which originates from the intensity modulation and reconstructs the RF signal. Without introducing electrical amplifiers, the RF power transmitted by the DL-RAU necessarily originates entirely from this time-varying photocurrent, and is under all circumstances limited by the RF power that is available for extraction from the photodetector. To maximize RF power extraction within the intended frequency band, the photodetector is interconnected to the antenna via a passive impedance matching network. Furthermore, the photodetector's bias voltage is chosen to be $0\,\mathrm{V}$, as is evident by the bias tee in Fig. 1a, such that a fully passive DL-RAU is obtained, powered solely by the optical signal. The main drawback of the proposed DL-RAU is its limited transmit power. While the transmitted power is increased by increasing the power of the RF signal that modulates the VCSEL, this will also increase nonlinear distortion by the VCSEL and photodetector. Moreover, the nonlinear distortion introduced by the photodetector is considerably enlarged in case of zero bias operation [38]. Therefore, to avoid significant nonlinear distortion degrading the link performance, the DL-RAU must be operated at low transmit power, limiting its useful communication range. However, when deploying the DL-RAU in attocells as small as $15\,\mathrm{cm} \times 15\,\mathrm{cm}$, propagation distances are extremely short, and the limited transmit power can be tolerated [3].

In a conventional active antenna design, the photodetector and antenna would be nearly directly interconnected, while the antenna input impedance is tuned to maximize power transfer. This direct matching requires no external matching network, but is difficult to achieve over a specific wide bandwidth, as in the intended application. Therefore, a safer approach is favored, where the antenna is matched to a reference resistance, and an external matching network efficiently transfers power from the photodetector to the antenna. Both subsystems are realized on separate PCBs, and a reference resistance of $50\,\Omega$ is selected, such that standard electrical SubMiniature version A (SMA) connectors can be used to validate the separate subsystems. The antenna is characterized by its return loss with respect to $50\,\Omega$, while the optoelectronic conversion circuit, being the photodetector, RF choke and matching network, is characterized by the S_{21} scattering parameter, with respect to the two port planes defined in Fig. 1a. The S_{21} transmission coefficient is defined as b_2/a_1, with b_2 the complex amplitude of the sinusoidal voltage wave scattered to port 2, being terminated by an impedance $R_{ref,2}$, when a generator with an internal impedance $R_{ref,1}$ injects a sinusoidal voltage wave with complex amplitude a_1 into port 1 [39]. Both reference impedances $R_{ref,1}$ and $R_{ref,1}$ are chosen to be $50\,\Omega$. A scattering parameter description is only valid in case the characterized circuit is linear, while the VCSEL and photodetector are nonlinear devices. When the power of the sinusoidal excitation is sufficiently small, the small-signal regime is in effect, and the behavior of these devices at their bias points is described by their linear small-signal equivalent circuit model. Within the small-signal regime, the complex values of S_{21} as a function of frequency are independent of the excitation power at port 1. As a result, the S_{21} scattering parameter offers a small-signal description of the entire optical link without assuming a specific modulation format or excitation power. This includes not only the optoelectronic conversion circuit, which is the subsystem under test, but also the VCSEL and the optical interconnection. As only the performance of the optoelectronic conversion circuit is of interest to this paper, it is useful to normalize the S_{21} scattering parameter with respect to all other parameters. To this end, S_{21} is simulated assuming a zero optical interconnection length (back-to-back connection) and an ideal VCSEL, whose input impedance equals $50\,\Omega$, as is shown in Fig. 1b. The ideal VCSEL's optical output power is modulated by the current i_m, indicated in Fig. 1b with a slope efficiency (SE) of $1\,\mathrm{W\,A^{-1}}$.

Fig. 3a offers an exploded view of the fully assembled DL-RAU, which consists of a stack of four separate two-layer PCBs, being two cavity PCBs consisting of $1.55\,\mathrm{mm}$ FR-4 substrates, the feed PCB and the slot PCB, each consisting of a $508\,\mu\mathrm{m}$ Rogers RO4350B high-frequency laminate. All eight copper layers have a thickness of $35\,\mu\mathrm{m}$. An identical pattern of non-plated vias is present on all four PCBs, serving as alignment holes. M3 screws are routed through all four PCBs to assemble them in one stack. This allows accurate alignment as well as a firm fixation to ensure electrical contact between the touching conducting layers of neighboring PCBs. These non-plated vias are located on the PCB edges where they have no influence on the functionality. The feed PCB contains the entire optoelectronic conversion circuit, while the remaining three PCBs compose the AFSIW antenna structure. The optoelectronic conversion circuit excites the antenna by means of a probe connecting the two outer conducting layers, as shown in Fig. 3a. Prior to assembly, both subsystems of the DL-RAU can be validated separately. To this end, the PCB containing the optoelectronic conversion circuit can be temporarily equipped with an SMA connector. To validate the antenna, another feed PCB is necessary, which temporarily replaces the feed PCB containing the optoelectronic conversion circuit in the stack shown in Fig. 3a. This auxiliary feed PCB contains a straight SMA connector, whose central conductor acts as the feed probe. The resulting stand-alone AFSIW antenna is shown in Fig. 3b. The following subsections focus on the two subsystems in greater detail.

B. Air-Filled Substrate-Integrated-Waveguide Cavity-Backed Slot Antenna

The adopted antenna topology is based on the conventional cavity-backed slot antenna [40], schematically outlined in Fig. 2. It consists of a hollow metallic cavity with a rectangular aperture. A feed line, such as a coaxial waveguide, supplies energy to the cavity, exciting electromagnetic fields that are confined by the metallic walls. Radiation of electromagnetic waves occurs through the aperture, which acts as a radiating slot. The antenna predominantly radiates in the frontal hemisphere ($z > 0$) with a high peak gain, and exhibits a high

Copyright (c) 2018 IEEE. Personal use is permitted. For any other purposes, permission must be obtained from the IEEE by emailing pubs-permissions@ieee.org.

This is the author's version of an article that has been published in this journal. Changes were made to this version by the publisher prior to publication.
The final version of record is available at http://dx.doi.org/10.1109/JLT.2018.2834153

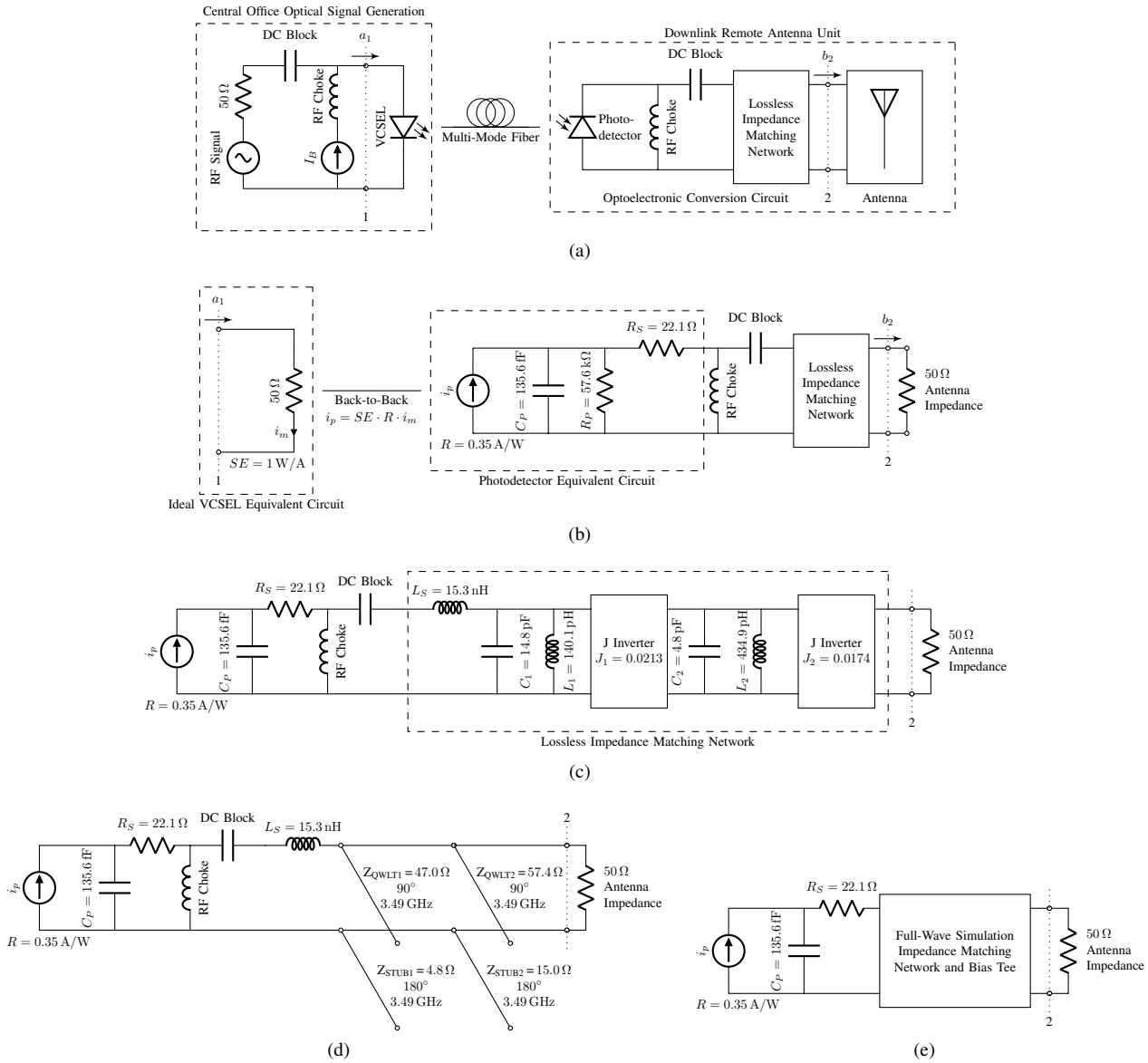

Fig. 1. Design evolution of the downlink remote antenna unit (DL-RAU): (a) high-level schematic overview of the adopted radio frequency over fiber scheme, (b) simulation model for the transmission coefficient S_{21} of the optical link, assuming sinusoidal small-signal modulation, including an ideal VCSEL with a slope efficiency SE of $1\,\mathrm{W\,A^{-1}}$ represented by its equivalent circuit, a back-to-back optical connection, and a photodetector with a responsivity R of $0.35\,\mathrm{A\,W^{-1}}$ represented by its equivalent circuit, (c) synthesis of an ideal lossless matching network, (d) implementation of the matching network using distributed elements, and (e) full-wave simulation of the matching network and bias tee.

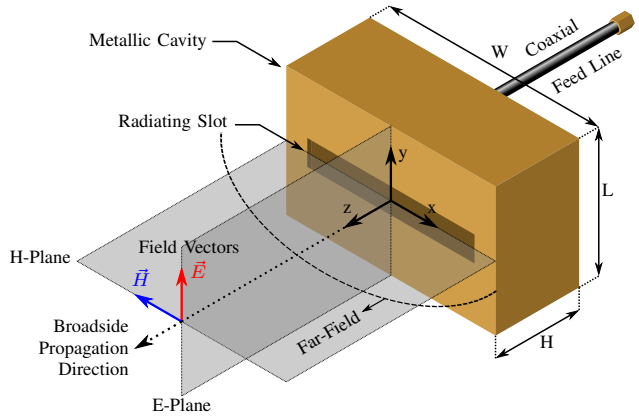

Fig. 2. The conventional coaxially-fed cavity-backed slot antenna topology.

radiation efficiency, a large front-to-back-ratio (FTBR, defined as the ratio of the gain in the $+z$ direction to the gain in the $-z$ direction), and a low cross-polarization level. As shown in Fig. 2, the YZ-plane contains the far-field's electric field vector and is referred to as the E-plane, whereas the XZ-plane contains the far-field's magnetic field vector and is referred to as the H-plane. Typically, the cavity depth H amounts to a quarter wavelength, resulting in a bulky antenna [41].

In [8], the cavity-backed slot antenna is implemented in AFSIW technology. The advantages of the conventional cavity-backed slot antenna, including a high gain, FTBR, and radiation efficiency are retained, while achieving a planar, low profile antenna. The AFSIW cavity-backed slot topology is schematically presented in Fig. 3b, and consists of an aligned stack of four separate two-layer PCBs, being two

Copyright (c) 2018 IEEE. Personal use is permitted. For any other purposes, permission must be obtained from the IEEE by emailing pubs-permissions@ieee.org.

This is the author's version of an article that has been published in this journal. Changes were made to this version by the publisher prior to publication.
The final version of record is available at http://dx.doi.org/10.1109/JLT.2018.2834153

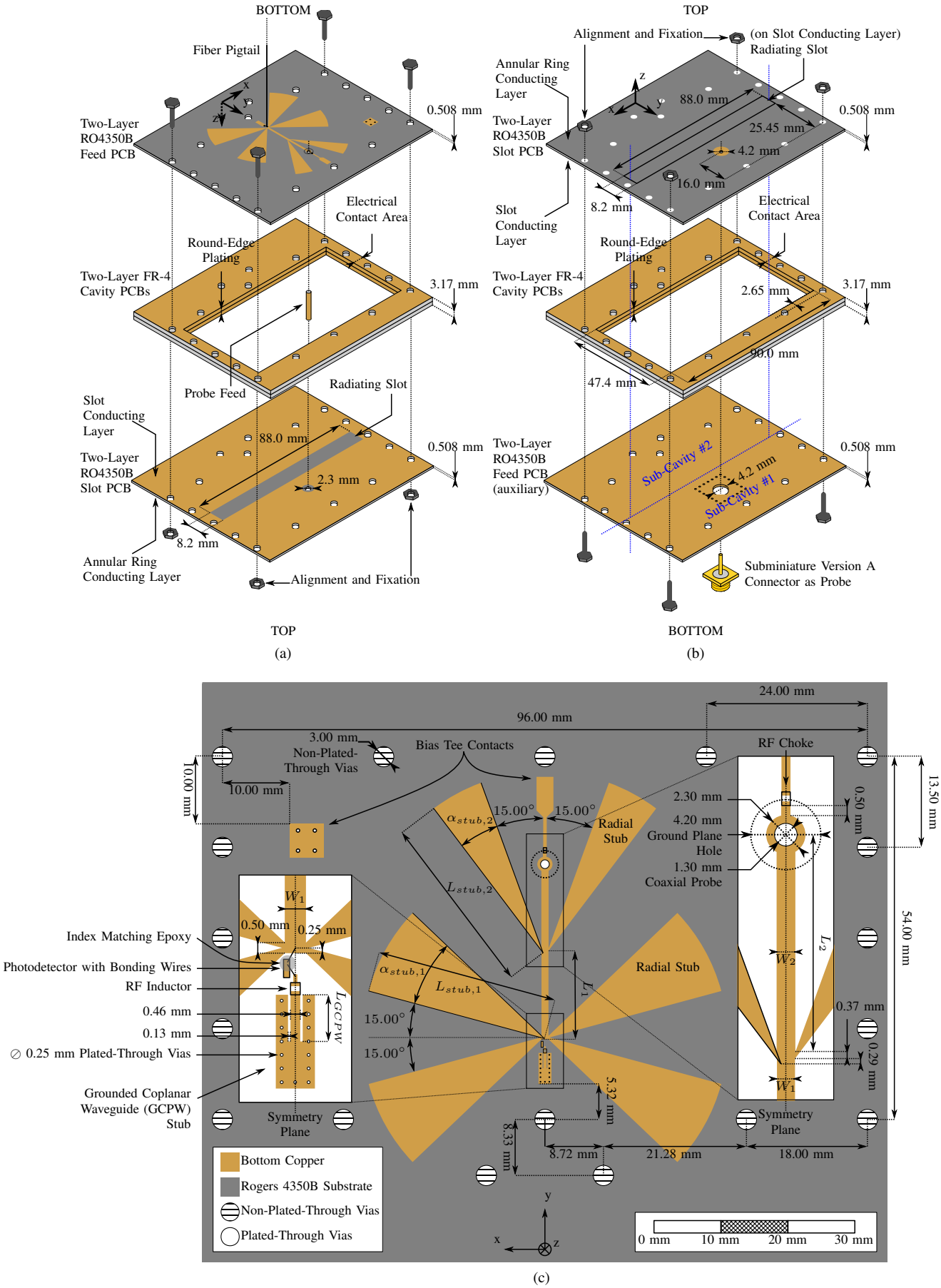

Fig. 3. (a) Exploded bottom view of the fully assembled downlink remote antenna unit. (b) Exploded top view of the air-filled substrate-integrated-waveguide cavity-backed slot antenna. (c) Detailed structure of the PCB that contains the optoelectronic conversion circuit.

Copyright (c) 2018 IEEE. Personal use is permitted. For any other purposes, permission must be obtained from the IEEE by emailing pubs-permissions@ieee.org.

This is the author's version of an article that has been published in this journal. Changes were made to this version by the publisher prior to publication.
The final version of record is available at http://dx.doi.org/10.1109/JLT.2018.2834153

cavity PCBs, the auxiliary feed PCB and the slot PCB. All PCBs are symmetrical with respect to the YZ-plane. The two FR-4 cavity PCBs are identical and contain, besides the non-plated vias intended for alignment, only a rectangular cavity with copper edge-plated sidewalls. These solid metal sidewalls ensure that the electromagnetic field does not penetrate the lossy FR-4 material. The top conducting layer of the feed PCB and the bottom conducting layer of the slot PCB cover the edge-plated cavity, implemented by the stacked edge-plated FR-4 PCBs, on both sides to form an air-filled rectangular cavity resonator. A capacitive feeding mechanism, similar to [42], is adopted. Figs. 3a and 3b show the slot PCB from a bottom and top perspective, respectively. Together, they provide a detailed view of the bottom and top conducting layers of the slot PCB, referred to as the slot conducting layer and annular ring conducting layer, respectively. The feed PCB contains a plated via with a diameter of $4.20\,\mathrm{mm}$, intended to introduce an SMA connector as probe to feed the cavity. The feed probe is electrically connected to a copper annular ring with a diameter of $4.20\,\mathrm{mm}$ on the annular ring conducting layer. A circular region with a diameter of $2.30\,\mathrm{mm}$ centered around the probe is removed from the slot conducting layer, such that no connection is made with the probe. The probe's RF currents excite the cavity through the capacitance between the annular ring conducting layer and the slot conducting layer. The radius of the annular ring can be used to tune this capacitance, serving as an extra degree of freedom when optimizing the antenna dimensions. The adopted feeding mechanism blocks DC currents and enables proper biasing, in our case $0\,\mathrm{V}$ biasing, of the photodetector. The slot conducting layer also contains a rectangular aperture acting as radiating element. This radiating slot has a length comparable to that of the SIW cavity, thereby splitting the cavity into two coupled sub-cavities. By letting both coupled sub-cavities resonate at a different frequency, a considerable impedance bandwidth is achieved [8]. The application of an air substrate further increases the impedance bandwidth and maximizes the radiation efficiency, at the cost of a slight increase in physical dimensions. Finally, the impedance bandwidth also increases when increasing the substrate thickness [8]. In the end, two $1.55\,\mathrm{mm}$ FR-4 PCBs enable the application of an air substrate that is thick enough to achieve a $-10\,\mathrm{dB}$ impedance bandwidth in the frequency band of interest. A more in-depth discussion of the antenna's operating principle can be found in [8].

The antenna structure is optimized in CST Microwave Studio 2017 using the frequency solver to match its input impedance to $50\,\Omega$ in a frequency bandwidth ranging from $3.10\,\mathrm{GHz}$ to $3.90\,\mathrm{GHz}$. This covers the entire RF signal band ($3.30\,\mathrm{GHz}$ – $3.70\,\mathrm{GHz}$) with adequate margins, such that robustness against fabrication inaccuracies is obtained. The optimized antenna dimensions are annotated in Fig. 3b. The simulated magnitude of the input reflection coefficient, shown in Fig. 4 by the dashed line, predicts a return loss (w.r.t. $50\,\Omega$) of over $13\,\mathrm{dB}$ within the RF signal band. The described antenna predominantly radiates in the upper hemisphere ($z > 0$), with a main lobe in the broadside direction ($+z$). The far field along broadside is linearly polarized with a cross-polarization level below $-60\,\mathrm{dB}$. The XZ- and the YZ-plane

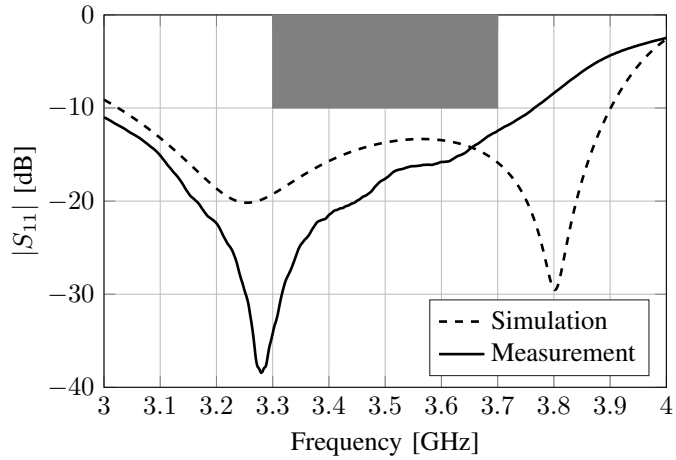

Fig. 4. Simulated and measured magnitude of the input reflection coefficient $|S_{11}|$ [dB] of the air-filled substrate-integrated-waveguide cavity-backed slot antenna, as a function of frequency.

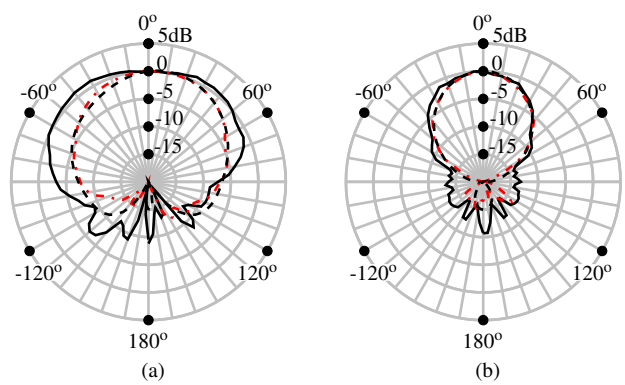

Fig. 5. Normalized free-space far-field gain patterns [dB] of the air-filled substrate-integrated-waveguide cavity-backed slot antenna (- - simulated, and - · - · measured) and the remote antenna unit (— measured) at the center frequency $3.50\,\mathrm{GHz}$, in (a) the E-plane, and (b) the H-plane.

contain the magnetic and electric field vector, respectively. Therefore, they are referred to as the H-plane and the E-plane, respectively. The far-field gain patterns at $3.50\,\mathrm{GHz}$ in the E- and H-plane are shown in Figs. 5a and 5b, respectively. These patterns are normalized w.r.t. the broadside direction. The simulation indicates a good FTBR of $15.0\,\mathrm{dB}$. The broadside gain as a function of frequency, shown in Fig. 6, remains almost constant at approximately $8.0\,\mathrm{dBi}$. Notwithstanding the applied bandwidth enhancement technique, the radiation properties remain stable over the full frequency range of operation.

C. Optoelectronic Conversion Circuit

Fig. 1b introduces the small-signal equivalent circuit of the biased photodetector. It consists of a parallel connection of a photocurrent source i_p, a resistance R_P, and a junction capacitance C_P, in series with a resistance R_S [36]. When the ideal VCSEL's output power is modulated by a sinusoidal current i_m and an optical back-to-back connection is assumed, the photocurrent is given by $i_p = SE \cdot R \cdot i_m$, with SE the

Copyright (c) 2018 IEEE. Personal use is permitted. For any other purposes, permission must be obtained from the IEEE by emailing pubs-permissions@ieee.org.

This is the author's version of an article that has been published in this journal. Changes were made to this version by the publisher prior to publication.
The final version of record is available at http://dx.doi.org/10.1109/JLT.2018.2834153

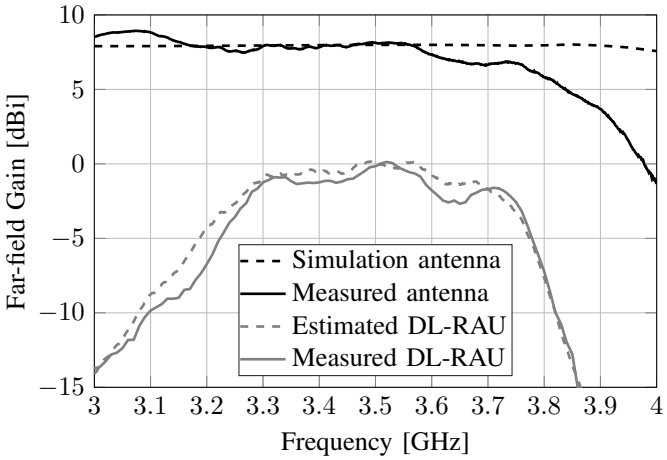

Fig. 6. Far-field broadside gain [dBi] of the air-filled substrate-integrated-waveguide cavity-backed slot antenna (simulation and measurement) and the remote antenna unit (estimation and measurement), as a function of frequency.

VCSEL's slope efficiency and R the photodetector's responsivity, as shown in Fig. 1b. Furthermore, the photodetector's internal impedance is given by

$$Z_{INT} = \frac{sC_P R_P R_S + R_S + R_P}{sC_P R_P + 1}, \tag{1}$$

with $s = j\omega$ and ω the angular frequency expressed in radians per second. When this circuit is loaded by an impedance equal to Z^*_{INT}, maximum power is extracted [39]. Hence, the maximum available power P_{AV} equals

$$P_{AV} = \frac{1}{8} \cdot \frac{R_P^2 |I_P|^2}{R_P + R_S + \omega^2 R_P^2 C_P^2 R_S}. \tag{2}$$

Its value decreases with increasing frequency. An impedance matching network is introduced between photodetector and antenna to increase the transducer gain G_T within the RF signal band. The transducer gain is defined as $G_T = P_A/P_{AV}$ [39], with P_A the power delivered to the antenna. We also define the impedance mismatch factor as $M = P_{MN,A}/P_{AV}$, where $P_{MN,A}$ is the power delivered to the matching network and antenna. In case of a lossless matching network, $P_A = P_{MN,A}$, and $G_T = M$. Evidently, to design the impedance matching network, we must first characterize the equivalent circuit element values.

The photodetector under study is a 25 Gbps 1x4 PIN photodiode array, requiring top illumination and yielding a peak responsivity near 0.85 µm. The device is packaged, exposing eight contacts with a 100 µm pitch, which are connected to a PCB through bonding wires. The package dimensions equal 1.0 mm × 0.4 mm × 0.1 mm. Only a single photodiode is required by the DL-RAU. A Keysight N5242A PNA-X Microwave Network Analyzer and a calibrated Picoprobe 40A-GS-100-DP microwave probe were used to measure the small-signal impedance of this device at 0 V bias from 2 GHz to 5 GHz in dark conditions. The equivalent circuit model element values, indicated in Fig. 1b, are obtained by minimizing the Euclidean distance between model impedance and measured impedance integrated over the full bandwidth. The parallel resistor R_P can be neglected, as its impedance is large compared to the capacitor C_P in the frequency band of interest. In addition, (2) shows that the available power changes by less than 10 % when removing R_P.

Therefore, the internal impedance of the photodetector simplifies to a series combination of a resistor and a capacitor, for which a Chebyshev impedance matching network is synthesized [35], [43]. This lossless reciprocal network maximizes the minimum transducer gain within a specified frequency interval, for the 50 Ω antenna impedance serving as a generator and the photodetector as a load [35]. Given reciprocity, the transducer gain will be identical when considering the photodetector as generator and the antenna as load.

To obtain maximal transducer gain within the full RF signal band, a third-order band-pass Chebyshev matching network is synthesized. The order was selected as a trade-off between transducer gain, ripple, complexity and losses. Fig. 1c, which focuses exclusively on the DL-RAU, shows that the synthesized matching network is lossless, and consists of an inductor (L_S), two shunt resonators ($L_1||C_1$ and $L_2||C_2$), and two admittance inverters (J_1 and J_2). The inductor L_S is placed in series with the photodetector, such that a series RLC resonator is formed. All three resonators have a resonance frequency of 3.49 GHz, being the geometrical center of the frequency band. An admittance inverter is defined as an ideal two-port that operates as a quarter-wavelength line of characteristic admittance J at all frequencies of interest [35]. All element values are annotated in Fig. 1c. The simulated transducer gain G_T and the normalized transmission coefficient magnitude $|S_{21}|$ are shown by the red dotted lines in Figs. 7a and 7b, respectively. A minimum transducer gain of 93.4 % and a normalized $|S_{21}|$ not smaller than 4.2 dB are observed within the pass-band. To simulate the normalized transmission coefficient magnitude $|S_{21}|$, an ideal VCSEL with an input impedance of 50 Ω and a slope efficiency of 1 W A^{-1}, a zero optical interconnection length, and a photodetector responsivity of 0.35 A W^{-1} are assumed. To put the performance of the synthesized matching network into perspective, a comparison is made with the case where the impedance matching network is omitted and the photodetector is directly loaded with the 50 Ω antenna. In this case, the simulated transducer gain G_T and the normalized $|S_{21}|$ are both much smaller as compared to when the matching network is present, as shown by the grey solid lines in Figs. 7a and 7b, respectively. A maximum transducer gain of 4.5 % and a maximum normalized transmission coefficient magnitude of −9.3 dB are observed within the pass-band, proving the synthesized matching network enhances the transmission by more than 13 dB.

An actual implementation of Fig. 1c with lumped components at 3.50 GHz is infeasible, due to extreme element values. Therefore, the shunt resonators and the J inverters are transformed to distributed elements, resulting in the circuit shown in Fig. 1d. The shunt resonators are transformed into open shunt stubs with an electrical length of 180° at their resonance frequency of 3.49 GHz. The characteristic impedance of each stub is calculated such that a susceptance slope at the resonance frequency is obtained that is identical to its lumped counterpart. Furthermore, actual quarter-wavelength lines with characteristic impedances $1/J_1$ and $1/J_2$ are used

Copyright (c) 2018 IEEE. Personal use is permitted. For any other purposes, permission must be obtained from the IEEE by emailing pubs-permissions@ieee.org.

This is the author's version of an article that has been published in this journal. Changes were made to this version by the publisher prior to publication.
The final version of record is available at http://dx.doi.org/10.1109/JLT.2018.2834153

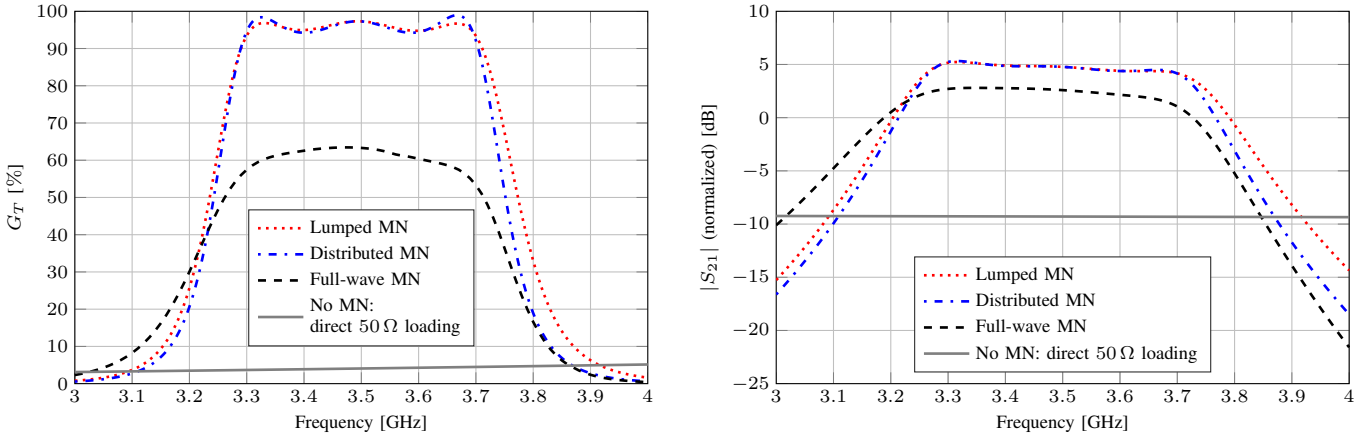

(a) (b)

Fig. 7. (a) Simulated transducer gain G_T [%] of the optoelectronic conversion circuit, as a function of frequency, and (b) simulated normalized transmission coefficient magnitude $|S_{21}|$ [dB] of the optical link, as a function of frequency, for the different design stages of the matching network (MN), using the models shown in Figs. 1c to 1e, which employ the ideal VCSEL model, and assume a back-to-back optical connection and a photodetector responsivity of $0.35\,\mathrm{A\,W^{-1}}$. The case of direct $50\,\Omega$ loading of the photodetector is also shown for comparison.

to realize the J inverters. During the synthesis of the matching network shown in Fig. 1c, there were two degrees of freedom originating from the J inverters with almost no impact on the performance. The first degree of freedom was exploited to fix the antenna impedance to $50\,\Omega$, while the second degree of freedom was used to fix the characteristic impedance of the second shunt stub to $15.0\,\Omega$. This results in quarter-wavelength lines with characteristic impedances quite close to $50\,\Omega$, enabling accurate fabrication. The simulated G_T and normalized $|S_{21}|$ (ideal VCSEL, back-to-back optical connection, photodetector responsivity of $0.35\,\mathrm{A\,W^{-1}}$) are shown by the blue dash-dotted lines in Figs. 7a and 7b, respectively. They indicate that the described transformations do not affect performance in a significant manner. A slightly worse minimum transducer gain of $92.1\,\%$ is observed within the pass-band, whereas the transmission coefficient magnitude remains almost unchanged.

In a final step, a microwave implementation of Fig. 1d is designed on the feed PCB, using the AFSIW antenna as platform. The conducting layer that simultaneously serves as the cavity's bottom plane and the matching network's ground plane is almost uninterrupted, apart from a hole with a diameter of $4.20\,\mathrm{mm}$ to allow for a coaxial connection to the antenna, as shown in Fig. 3c. For now, we assume that an SMA connector is mounted on the backside of the PCB on this position. The feed PCB is depicted schematically in Fig. 3c, indicating all important dimensions and details. The entire structure is designed in CST Microwave Studio 2017, with the coaxial connector serving as excitation port.

The photodetector is glued onto the PCB with its contacts and active region facing upward. The contacts are connected to the PCB by means of two aluminum bonding wires with a diameter of $25\,\mu\mathrm{m}$. In a top view, shown in Fig. 3c, the bonding wires follow a straight path. They bridge a distance of $750\,\mu\mathrm{m}$ and make an angle of $30°$ with respect to the symmetry plane indicated by the dotted line. The actual bonding wires are applied manually, giving rise to some uncertainty regarding their exact path and height profile. The bonding wires are modeled through a spline geometry, reaching a maximum height above the PCB of $150\,\mu\mathrm{m}$ halfway. The effect of the bonding wires is predominantly inductive, contributing to the series inductor L_S. Yet, they also add some series resistance, leading to additional losses.

A major contribution to L_S is provided by a $7.2\,\mathrm{nH}$ chip inductor component of the Coilcraft 0201DS Series. A final contribution to L_S is supplied by an electrically short grounded coplanar waveguide (GCPW) stub, terminated by a short. Its input impedance equals $Z_{GCPW} = jZ_c \tan(kd)$, where Z_c is the characteristic impedance, k the wavenumber and d the length. Therefore, by tuning the length of the shorted GCPW, the total inductance can be tuned. In the actual prototype, the position of the short is adjusted by applying copper tape. In Fig. 3c, the GCPW is shorted halfway, as this proves to be the optimal position according to full-wave simulation, which takes all sources of inductance into account. Starting from this position, the length can be increased or decreased by $2\,\mathrm{mm}$, which would add or remove approximately $0.5\,\mathrm{nH}$ of inductance. This tunable inductor was added to increase the robustness of the design against manufacturing tolerances on the chip inductor, as well as uncertainty on the bonding wire profiles.

To implement the $180°$ open shunt stubs of Fig. 1d with a characteristic impedance as low as $4.8\,\Omega$ and $15.0\,\Omega$, shunt radial stubs are applied [44]. As shown in Fig. 3c, the lower impedance shunt stub is realized as four parallel radial stubs, while the higher impedance shunt stub is realized as two shunt connected radial stubs. The angular distance between the stubs is kept sufficiently high, such that no significant coupling occurs between the stubs.

Furthermore, a bias tee is included near the antenna probe. While the antenna could be designed to offer a very low DC resistance, so that the antenna biases the photodetector at $0\,\mathrm{V}$ without requiring a bias tee, this would remove the possibility of measuring the DC photocurrent, and thus the photodetector

Copyright (c) 2018 IEEE. Personal use is permitted. For any other purposes, permission must be obtained from the IEEE by emailing pubs-permissions@ieee.org.

This is the author's version of an article that has been published in this journal. Changes were made to this version by the publisher prior to publication.
The final version of record is available at http://dx.doi.org/10.1109/JLT.2018.2834153

responsivity, once the antenna and optoelectronic conversion circuit are integrated. The photodetector responsivity is a parameter with a major impact on the transmission coefficient magnitude $|S_{21}|$ and, therefore, this dedicated bias tee is essential for the validation of the DL-RAU. A $34.0\,\mathrm{nH}$ chip inductor of the Coilcraft 0302CS Series is therefore used as an RF choke. This dedicated bias tee also enables active alignment during attachment of the fiber pigtail. This involves positioning the cleaved end of the fiber close to the active region of the photodetector, while exciting the other end of the fiber with an appropriate light source, and gluing the cleaved end to that location where the maximum photocurrent is observed. Using this technique, an OM2 multi-mode fiber pigtail is attached to the photodetector with an ultra-violet (UV) light-cured epoxy (EPO-TEK OG142-112). The epoxy sits around the bonding wires, and will, therefore, have some influence on the operation of the matching network. This is taken into account in the simulation model by including a cylinder of epoxy material centered at the used photodetector contacts, as indicated in Fig. 3c. The cylinder has a diameter of $1.6\,\mathrm{mm}$ and a height of $0.5\,\mathrm{mm}$. The dielectric constant of the cured epoxy material was estimated to be 3.

Full-wave optimization of the matching network is performed using the frequency solver of CST Microwave Studio 2017, to maximize G_T within the RF signal band ranging from $3.30\,\mathrm{GHz}$ to $3.70\,\mathrm{GHz}$. The optimized parameters are listed in Table I. Both the initial and optimized dimensions are given. The resulting simulated G_T and $|S_{21}|$ (ideal VCSEL, back-to-back optical connection, photodetector responsivity of $0.35\,\mathrm{A\,W^{-1}}$) are shown in Figs. 7a and 7b by the black dashed lines. A minimum transducer gain of $53.3\,\%$ and a minimum normalized $|S_{21}|$ of $1.1\,\mathrm{dB}$ are observed within the pass-band. These results are somewhat degraded as compared to the ones obtained for the ideal circuit of Fig. 1d. For the largest part, this degradation is caused by the inclusion of all losses in the simulation. However, the transducer gain is degraded more than can be explained by the inclusion of losses alone. The full-wave simulation also takes the specific implementation of the matching network into account, which involves the transition from the photodetector to the microstrip lines with bonding wires, and the transition from microstrip lines to the probe, further reducing the impedance mismatch factor and transducer gain by about $10\,\%$, as compared to the values obtained for the ideal distributed circuit of Fig. 1d.

A detailed power analysis is conducted of the optimized optoelectronic conversion circuit. The impedance mismatch factor and the transducer gain are both calculated as a function of frequency. Within the RF signal band, an average impedance mismatch factor of $81.3\,\%$ and an average transducer gain of $60.9\,\%$ are obtained. The transducer gain takes matching network losses into account, and, as a consequence, is lower than the impedance mismatch factor. The contributions of the different loss mechanisms, including radiation loss (on average $4.5\,\%$), substrate loss (on average $4.0\,\%$), bonding wire conduction loss (on average $0.7\,\%$), copper conduction loss (on average $3.0\,\%$), chip inductor conduction loss (on average $8.1\,\%$), and bias tee loss (on average $0.1\,\%$), are also quantified. The result is shown in Fig. 8. Extensive simulations suggest that starting from a third-order matching network and further increasing the order would, as expected, improve the impedance mismatch factor. However, the losses associated with the additional matching network sections would nullify the potential gain in performance. Therefore, a third-order matching network is selected.

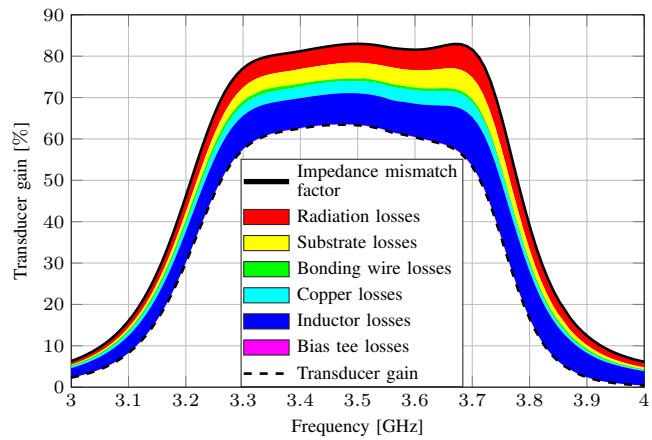

Fig. 8. Simulation of the power losses occurring in the optoelectronic conversion circuit and its components.

TABLE I
OPTOELECTRONIC CONVERSION CIRCUIT DIMENSIONS BEFORE AND AFTER OPTIMIZATION

Dimension	Optimized	Preliminary
L_{GCPW} [mm]	2.00	2.00
$L_{stub,1}$ [mm]	26.97	27.05
$\alpha_{stub,1}$ [°]	28.69	36.00
L_1 [mm]	13.17	12.71
W_1 [mm]	1.03	1.19
$L_{stub,2}$ [mm]	26.82	27.50
$\alpha_{stub,2}$ [°]	17.10	21.10
L_2 [mm]	12.50	12.90
W_2 [mm]	1.07	0.85

III. VALIDATION AND MEASUREMENTS

The two subsystems of the DL-RAU, being the optoelectronic conversion circuit and the AFSIW antenna, are prototyped and first characterized separately. These measurements allow to predict the performance when combining both subsystems to form the DL-RAU. Finally, the fully assembled DL-RAU is characterized and the adopted co-design strategy is validated.

Both the AFSIW antenna and the DL-RAU are characterized by means of an Orbit/FR DBDR antenna positioning system, connected to the network analyzer, inside an anechoic chamber mimicking free-space conditions. Far-field gain patterns are evaluated with the gain comparison method using a calibrated ultra-wideband horn antenna located in the far-field of the antenna under test. Table II summarizes the most important far-field results at $3.50\,\mathrm{GHz}$, including the broadside gain, the FTBR, the broadside cross-polarization level, and the $3\,\mathrm{dB}$ beam widths in both the E- and H-plane (here defined as the angle between the points on the main lobe where gain has decreased by $3\,\mathrm{dB}$ w.r.t. maximum gain).

Copyright (c) 2018 IEEE. Personal use is permitted. For any other purposes, permission must be obtained from the IEEE by emailing pubs-permissions@ieee.org.

This is the author's version of an article that has been published in this journal. Changes were made to this version by the publisher prior to publication.
The final version of record is available at http://dx.doi.org/10.1109/JLT.2018.2834153

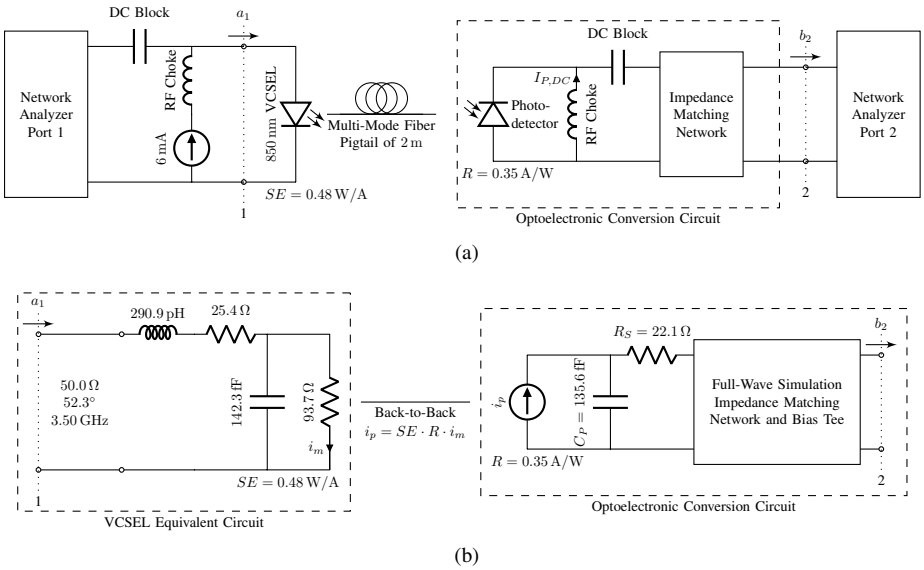

Fig. 9. (a) Measurement setup for the transmission coefficient magnitude $|S_{21}|$ of the optical link: the 850 nm VCSEL, biased at 6 mA (quiescent optical power of 4.47 dBm), is directly modulated by a sinusoidal excitation under small-signal conditions by network analyzer port 1, the VCSEL's output is connected to the optoelectronic conversion circuit using its 2-meter long multi-mode fiber pigtail, and the output of the optoelectronic conversion circuit is connected to network analyzer port 2. (b) Simulation model for the transmission coefficient magnitude $|S_{21}|$ of the optical link assuming sinusoidal small-signal modulation: VCSEL with a slope efficiency SE of $0.48\,\mathrm{W\,A^{-1}}$ represented by its equivalent circuit (characterized at 6 mA bias), back-to-back optical connection, photodetector with a responsivity R of $0.35\,\mathrm{A\,W^{-1}}$ represented by its equivalent circuit (characterized at 0 V bias).

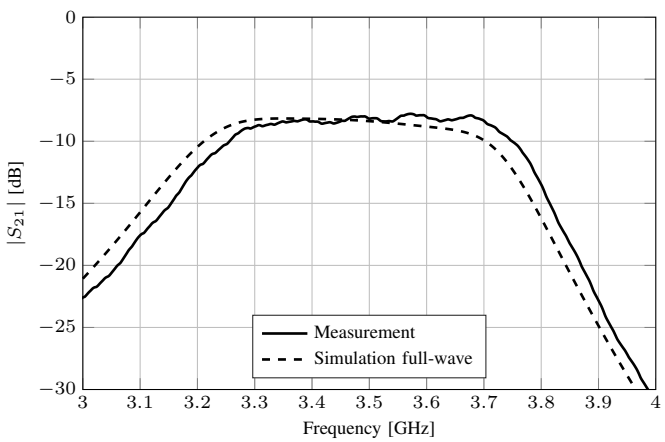

Fig. 10. Measured and simulated transmission coefficient magnitude $|S_{21}|$ [dB] of the optical link, as a function of frequency, using the measurement setup shown in Fig. 9a and the simulation model shown in Fig. 9b, respectively.

TABLE II
MEASURED (SIMULATED) FAR-FIELD RADIATION PATTERN CHARACTERISTICS AT 3.50 GHZ FOR THE AFSIW ANTENNA AND THE DL-RAU.

Characteristic	AFSIW Antenna	DL-RAU
Broadside Gain [dBi]	8.1 (8.0)	-0.2 (0.0)
FTBR [dB]	20.0 (15.0)	8.8 (–)
Cross-polarization level [dB]	-45.4 (-63.1)	-28.8 (–)
E-plane beam width [°]	95 (85)	150 (–)
H-plane beam width [°]	50 (50)	55 (–)

A. Air-Filled Substrate-Integrated-Waveguide Cavity-Backed Slot Antenna

Fig. 4 compares the simulated and measured input reflection coefficient magnitude of the AFSIW antenna in free-space conditions. A return loss (w.r.t. 50 Ω) of more than 12.4 dB is measured over the entire RF signal band. The deviation between measurement and simulation is attributed to the fabrication tolerances associated with the edge-plating used to form the cavity. The measured far-field radiation characteristics at 3.50 GHz show an excellent agreement with the simulated ones, as is evident from Table II. The measured (red dash-dotted line) and simulated (black dashed line) normalized far-field gain patterns at 3.50 GHz in the E- and H-planes agree very well, as shown in Figs. 5a and 5b. Finally, Fig. 6 shows that the measured broadside gain as a function of frequency (black dashed line) agrees with the simulation (black solid line) to within 1.3 dB in the entire RF signal band. At higher frequencies, the deviation between simulation and measurement increases, which can be explained by a radiation pattern null around 4.2 GHz that is shifted down as a result of fabrication inaccuracies.

B. Optoelectronic Conversion Circuit

A prototype of the optoelectronic conversion circuit, shown in Fig. 11a, is characterized by measuring the transmission coefficient S_{21} with the vector network analyzer (VNA). The measurement setup is depicted schematically in Fig. 9a. A V50-850M 850 nm multi-mode VCSEL, biased at a current of 6 mA, is employed as a light source. At this bias current, a quiescent optical output power of 4.47 dBm and a slope efficiency of $0.48\,\mathrm{W\,A^{-1}}$ are measured with an optical power meter. The optical output of the biased VCSEL is connected to

Copyright (c) 2018 IEEE. Personal use is permitted. For any other purposes, permission must be obtained from the IEEE by emailing pubs-permissions@ieee.org.

This is the author's version of an article that has been published in this journal. Changes were made to this version by the publisher prior to publication.
The final version of record is available at http://dx.doi.org/10.1109/JLT.2018.2834153

the 2-m long multi-mode fiber pigtail of the DL-RAU. The resulting DC photocurrent $I_{P,DC}$ is measured with the dedicated bias tee of the DL-RAU, and amounts to $0.97\,\mathrm{mA}$, leading to a photodetector responsivity of $0.35\,\mathrm{A\,W^{-1}}$. This responsivity takes all optical losses into account, including connector loss, fiber attenuation, and loss occurring when coupling the light into the photodetector. Considering the short length of the pigtail, the coupling loss is dominant. When comparing this responsivity value to the photodetector's nominal value of $0.55\,\mathrm{A\,W^{-1}}$, it can be concluded that the attached fiber pigtail achieves a coupling efficiency of $63.6\,\%$. Furthermore, when comparing with the theoretical limit at $850\,\mathrm{nm}$ of $0.69\,\mathrm{A\,W^{-1}}$, which is obtained for a photodetector with a $100\,\%$ quantum efficiency [5], it can be concluded that a coupling efficiency of at least $51\,\%$ is achieved. Port 1 of the VNA is connected to the VCSEL through an external bias tee, such that the sinusoidal excitation of the VNA modulates the VCSEL's output power. Finally, port 2 of the VNA is connected to the output of the optoelectronic conversion circuit. The VNA is calibrated with respect to its port planes, as indicated in Fig. 9a.

The resulting measurement of the transmission coefficient magnitude $|S_{21}|$ cannot be compared to the simulated ones shown in Fig. 7b, as these simulations were performed using an ideal VCSEL model. A more accurate simulation model is depicted in Fig. 9b, which includes a small-signal equivalent circuit model for the VCSEL at a bias current of $6\,\mathrm{mA}$, such that validation of the measurement is possible. Specifically, the model proposed in [45] was used. A resistance of $93.7\,\Omega$ in parallel with a capacitance of $142.3\,\mathrm{fF}$ represents the junction, while the series resistance of $25.4\,\Omega$ represents the metal contacts and the resistance of the Bragg mirror stack [46]. The VCSEL's optical output power is modulated by the current i_m, indicated in Fig. 9b, with the slope efficiency measured at $0.48\,\mathrm{W\,A^{-1}}$. A parasitic inductor of $290.9\,\mathrm{pH}$, arising from the contacts, is added in series. The model proposed in [45] includes additional parasitic components as well as an additional inductor, but these prove to be negligible at a modulation frequency up to $4\,\mathrm{GHz}$. Finally, a $50\,\Omega$ transmission line with an electrical length of $52.3°$ at $3.50\,\mathrm{GHz}$ is included, which models the $1.85\,\mathrm{mm}$ coaxial connector of the modulation input. The $|S_{21}|$ is simulated assuming a zero optical interconnection length (back-to-back connection) and a photodetector responsivity of $0.35\,\mathrm{A\,W^{-1}}$.

Fig. 10 compares the resulting measurement (black solid line) and simulation (black dashed line), and reveals an excellent agreement. A maximum insertion loss of $8.8\,\mathrm{dB}$ is measured over the entire RF signal band, which compares favorably with the simulated maximum insertion loss of $9.9\,\mathrm{dB}$. The slight deviation between measurement and simulation is caused by several reasons. Foremost, the length of the shorted GCPW stub, contributing to the inductance L_S, is shortened to a length of $0.5\,\mathrm{mm}$ to achieve a flatter $|S_{21}|$ characteristic in the RF signal band. In this way, an insertion loss of $8.8\,\mathrm{dB}$ and $8.4\,\mathrm{dB}$ is obtained at $3.30\,\mathrm{GHz}$ and $3.70\,\mathrm{GHz}$, respectively. Furthermore, inaccuracies on the element values of the photodetector's equivalent circuit will have a slight impact. Finally, the index-matching epoxy used for fiber pigtailing was taken into account using a simplified geometry and estimation of its dielectric constant.

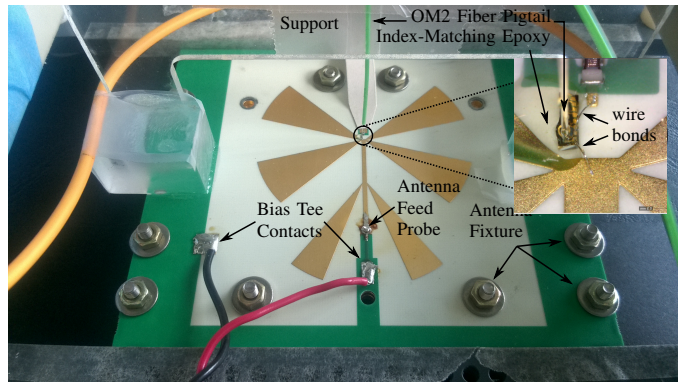

(a)

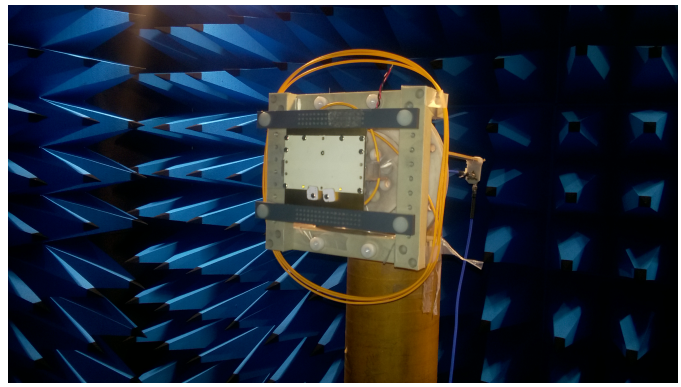

(b)

Fig. 11. (a) Prototype of the optoelectronic conversion circuit. (b) Fully assembled downlink remote antenna unit prototype deployed in the anechoic chamber.

C. Full Downlink Remote Antenna Unit

1) Far-Field Radiation Pattern: The subsystems which were characterized in the previous subsections are now assembled to form the full DL-RAU, shown after being mounted in the anechoic chamber in Fig. 11b. The same measurement conditions as in the previous subsection, being a VCSEL bias current of $6\,\mathrm{mA}$, a VCSEL slope efficiency of $0.48\,\mathrm{W\,A^{-1}}$, and a photodetector responsivity of $0.35\,\mathrm{A\,W^{-1}}$ apply. It is important to note that the reference plane for measuring the radiation pattern is located at the modulation input of the VCSEL. Figs. 5a and 5b present the far-field gain patterns measured in the E- and H-plane at $3.50\,\mathrm{GHz}$. Also evident in Table II, the measured radiation patterns of the DL-RAU and the AFSIW antenna show a good agreement. The FTBR and cross-polarization level are somewhat degraded. However, the measured beam width in the E-plane is considerably wider. This is caused by the additional hardware needed in proximity of the DL-RAU during measurement of the radiation pattern, such as the VCSEL and the wound up fiber pigtail. Naturally, the E-plane beam width will be more affected than the H-plane one, considering that the beam width is already very broad in this plane, compared to the H-plane. The measured broadside gain as a function of frequency is presented in Fig. 6 (grey solid line). It reaches a peak of $0.13\,\mathrm{dBi}$ at $3.52\,\mathrm{GHz}$. The

Copyright (c) 2018 IEEE. Personal use is permitted. For any other purposes, permission must be obtained from the IEEE by emailing pubs-permissions@ieee.org.

This is the author's version of an article that has been published in this journal. Changes were made to this version by the publisher prior to publication.
The final version of record is available at http://dx.doi.org/10.1109/JLT.2018.2834153

gain remains stable to within $-3\,\mathrm{dB}$ in a frequency range from $3.26\,\mathrm{GHz}$ to $3.76\,\mathrm{GHz}$. The co-design strategy is validated by assessing whether the DL-RAU performs as expected from the performance of the subsystems. The expected broadside gain as a function of frequency for the DL-RAU is estimated by adding the measured transmission coefficient magnitude of the optoelectronic conversion circuit (shown in Fig. 10), expressed in dB, to the broadside gain of the AFSIW antenna (shown in Fig. 6), expressed in dBi. The result is shown in Fig. 6 (grey dashed line), and does not deviate from the measured values (grey solid line) by more than $1.3\,\mathrm{dB}$ over the entire RF signal band. The deviation is explained by additional impedance mismatch between the two subsystems, as the antenna is not perfectly matched to $50\,\Omega$.

2) Link Measurement: As a final validation, a unidirectional data link is set up in the anechoic chamber between the DL-RAU, serving as transmit antenna, and the AFSIW antenna, serving as receive antenna. The measurement setup is shown in Fig. 12a. The antennas are aligned, such that each antenna has its broadside direction aimed toward the phase center of the other antenna, along the z-axis, with parallel radiating slots and a separation of $20\,\mathrm{cm}$. As the largest dimension of both antennas amounts to $13.4\,\mathrm{cm}$, the boundary between the reactive near-field region and the radiative near-field region is estimated at a distance of $10.3\,\mathrm{cm}$ at $3.50\,\mathrm{GHz}$, while the Fraunhofer far-field region is estimated to begin at a distance of $41.7\,\mathrm{cm}$ [47]. As a result, the two antennas are in each other's radiative near-field region. The VCSEL, connected to the DL-RAU, is now biased with a $4\,\mathrm{mA}$ current, and is directly modulated by a quadrature-amplitude-modulated (QAM) signal with a carrier frequency of $3.50\,\mathrm{GHz}$ and a power of $-15\,\mathrm{dBm}$, which is generated by an Anritsu MG3710A Vector Signal Generator (VSG). The VCSEL's bias current was reduced from $6\,\mathrm{mA}$ to $4\,\mathrm{mA}$ because linearity is found to be superior in this region [37]. Such a short propagation distance and low transmission power are relevant for novel ultra-high density wireless communication systems, as proposed in [3], which require massive amounts of RAUs, deployed in attocells as small as $15\,\mathrm{cm} \times 15\,\mathrm{cm}$. The QAM signal has a constellation size of 64 symbols (64-QAM) and achieves a symbol rate of $80\,\mathrm{MBd}$, which is the maximum offered by the VSG. The signal received by the AFSIW antenna is immediately amplified by a Mini-Circuits ZX60-83LN-S+ Low Noise Amplifier (powered with $5\,\mathrm{V}$) and demodulated by an Anritsu MS2692A Signal Analyzer, which calculates the root-mean-square error-vector-magnitude (rms EVM). The transmitter and receiver apply a root-raised-cosine filter with a roll-off factor of 0.3. The constellation diagram after demodulation is shown in Fig. 12b. The data link performs excellently, with an rms EVM of only $2.2\,\%$ ($-33.15\,\mathrm{dB}$), which proves that the DL-RAU can transmit a data signal of at least $480\,\mathrm{Mbps}$ with an equivalent isotropic radiated power (EIRP) of at least $-15\,\mathrm{dBm}$ without introducing significant distortion. This EIRP value of $-15\,\mathrm{dBm}$ is calculated by adding the $-15\,\mathrm{dBm}$ power of the QAM signal to the far-field gain of the DL-RAU, which amounts to approximately $0\,\mathrm{dBi}$.

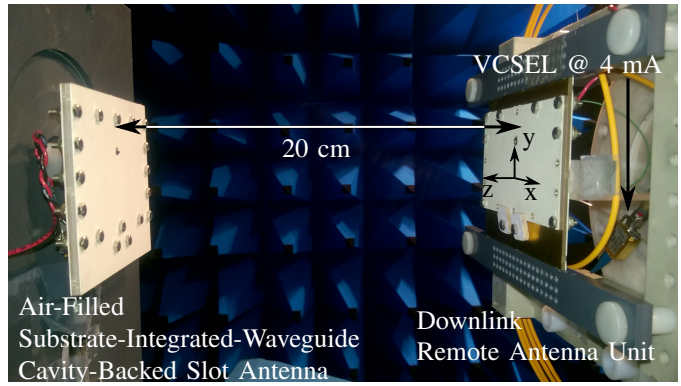

(a)

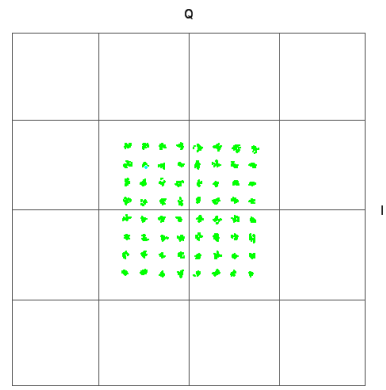

(b)

Fig. 12. (a) Unidirectional data link from the proposed downlink remote antenna unit (transmitter, right) to the AFSIW antenna (receiver, left) over a distance of $20\,\mathrm{cm}$, set up in an anechoic chamber. (b) Constellation diagram after demodulation: 64-QAM digital modulation scheme at a symbol rate of $80\,\mathrm{MBd}$ ($480\,\mathrm{Mbps}$). An excellent link quality with an rms EVM of only $2.2\,\%$ is observed.

IV. Conclusion and Outlook

In this paper, a fully passive DL-RAU that is entirely powered by a single optical fiber, was proposed. An effective co-design strategy was devised, which resulted in a compact, cost-effective, and energy-efficient unit, serving as an ideal building block for novel, highly specialized, ultra-high density wireless communication systems, which require massive amounts of remote antenna units, deployed in attocells as small as $15\,\mathrm{cm} \times 15\,\mathrm{cm}$. The key design decisions that led to these properties were operating the photodetector at zero bias voltage and omitting additional active components, while maximizing the power transfer from the photodetector to the AFSIW antenna by means of an impedance matching network, compactly integrated on the backside of the antenna. As a next step, scaling of the concept to mmWave frequencies is of great interest. More application-specific photodiodes with higher built-in electric field could be selected to improve zero bias operation [20]. Furthermore, the input impedance of the antenna itself could be tuned to match the impedance of the photodiode, such that no external matching network is necessary and a more compact unit is obtained. Finally, by applying a lower-order impedance matching network, while adopting a miniaturized antenna topology as proposed in [48], an even more compact unit could be obtained. Multiple measurements

Copyright (c) 2018 IEEE. Personal use is permitted. For any other purposes, permission must be obtained from the IEEE by emailing pubs-permissions@ieee.org.

This is the author's version of an article that has been published in this journal. Changes were made to this version by the publisher prior to publication.
The final version of record is available at http://dx.doi.org/10.1109/JLT.2018.2834153

performed on a prototype in an anechoic chamber, including radiation pattern measurements and data link measurements, validate its performance. The main disadvantage of the proposed DL-RAU is its limited transmit power. This restriction is required to avoid nonlinear distortion introduced by the VCSEL and photodetector. In a possible solution, the DL-RAU contains multiple photodetectors, each illuminated by an optical fiber, and their power is combined on the antenna [49] to increase the transmitted power.

Acknowledgment

The authors would like to thank the Centre for Microsystems Technology (CMST) and its expertise centre Namifab at Ghent University, particularly Dr. Björn Vandecasteele and Prof. Jeroen Missine, for their skillful help during assembly of the prototypes. Prof. Piet Demeester thanks the ERC for his advanced grant 695495 "ATTO: A new concept for ultrahigh capacity wireless networks".

References

[1] C. Lim, A. Nirmalathas, M. Bakaul, P. Gamage, K. L. Lee, Y. Yang, D. Novak, and R. Waterhouse, "Fiber-Wireless Networks and Subsystem Technologies," *Journal of Lightwave Technology*, vol. 28, pp. 390–405, Feb 2010.

[2] D. Novak, R. B. Waterhouse, A. Nirmalathas, C. Lim, P. A. Gamage, T. R. Clark, M. L. Dennis, and J. A. Nanzer, "Radio-Over-Fiber Technologies for Emerging Wireless Systems," *IEEE Journal of Quantum Electronics*, vol. 52, pp. 1–11, Jan 2016.

[3] G. Torfs, H. Li, S. Agneessens, J. Bauwelinck, L. Breyne, O. Caytan, W. Joseph, S. Lemey, H. Rogier, A. Thielens, D. Vande Ginste, J. Van Kerrebrouck, G. Vermeeren, X. Yin, and P. Demeester, "ATTO: Wireless Networking at Fiber Speed," *Journal of Lightwave Technology*, vol. 36, pp. 1468–1477, April 2018.

[4] B. Lannoo, A. Dixit, D. Colle, J. Bauwelinck, B. Dhoedt, B. Jooris, I. Moerman, M. Pickavet, H. Rogier, P. Simoens, G. Torfs, D. Vande Ginste, and P. Demeester, "Radio-over-fibre for ultra-small 5G cells," in *2015 17th International Conference on Transparent Optical Networks (ICTON)*, pp. 1–4, July 2015.

[5] G. P. Agrawal, *Fiber-Optic Communication Systems*. John Wiley & Sons, Inc., 4 ed., 2011.

[6] Federal Communications Commission, "Order on Reconsideration and Second Report and Order, GN Docket No. 12-354," released May 2, 2016.

[7] A. Belenguer, H. Esteban, and V. E. Boria, "Novel Empty Substrate Integrated Waveguide for High-Performance Microwave Integrated Circuits," *IEEE Transactions on Microwave Theory and Techniques*, vol. 62, pp. 832–839, April 2014.

[8] Q. Van den Brande, S. Lemey, J. Vanfleteren, and H. Rogier, "Highly-Efficient Impulse-Radio Ultra-Wideband Cavity-Backed Slot Antenna in Stacked Air-Filled Substrate-Integrated-Waveguide Technology," *IEEE Transactions on Antennas and Propagation*, vol. 66, pp. 2199–2209, May 2018.

[9] J. V. Morro, A. Rodríguez, A. Belenguer, H. Esteban, and V. Boria, "Multilevel transition in empty substrate integrated waveguide," *Electronics Letters*, vol. 52, no. 18, pp. 1543–1544, 2016.

[10] A. Belenguer, J. L. Cano, H. Esteban, E. Artal, and V. E. Boria, "Empty substrate integrated waveguide technology for E plane high-frequency and high-performance circuits," *Radio Science*, vol. 52, no. 1, pp. 49–69, 2017.

[11] J. Mateo, A. M. Torres, A. Belenguer, and A. L. Borja, "Highly Efficient and Well-Matched Empty Substrate Integrated Waveguide H-Plane Horn Antenna," *IEEE Antennas and Wireless Propagation Letters*, vol. 15, pp. 1510–1513, 2016.

[12] D. Wake, A. Nkansah, and N. Gomes, "Optical Powering of Remote Units for Radio over Fiber Links," in *2007 International Topical Meeting on Microwave Photonics*, pp. 29–32, Oct 2007.

[13] D. Wake, A. Nkansah, N. J. Gomes, C. Lethien, C. Sion, and J. P. Vilcot, "Optically Powered Remote Units for Radio-Over-Fiber Systems," *Journal of Lightwave Technology*, vol. 26, pp. 2484–2491, Aug 2008.

[14] D. H. Thomas, G. V. de Faria, and J. P. von der Weid, "Fully powered-over-fibre remote antenna unit," in *2008 International Topical Meeting on Microwave Photonics jointly held with the 2008 Asia-Pacific Microwave Photonics Conference*, pp. 102–105, Sept 2008.

[15] D. Wake, N. J. Gomes, C. Lethien, C. Sion, and J. P. Vilcot, "An optically powered radio over fiber remote unit using wavelength division multiplexing," in *2008 International Topical Meeting on Microwave Photonics jointly held with the 2008 Asia-Pacific Microwave Photonics Conference*, pp. 197–200, Sept 2008.

[16] C. Lethien, D. Wake, B. Verbeke, J. P. Vilcot, C. Loyez, M. Zegaoui, N. Gomes, N. Rolland, and P. A. Rolland, "Energy-Autonomous Picocell Remote Antenna Unit for Radio-Over-Fiber System Using the Multiservices Concept," *IEEE Photonics Technology Letters*, vol. 24, pp. 649–651, April 2012.

[17] M. Matsuura and J. Sato, "Bidirectional Radio-Over-Fiber Systems Using Double-Clad Fibers for Optically Powered Remote Antenna Units," *IEEE Photonics Journal*, vol. 7, pp. 1–9, Feb 2015.

[18] Y. Minamoto and M. Matsuura, "Optically controlled beam steering system with 60-W power-over-fiber feed for remote antenna units," in *2016 Optical Fiber Communications Conference and Exhibition (OFC)*, pp. 1–3, March 2016.

[19] M. Matsuura and Y. Minamoto, "Optically Powered and Controlled Beam Steering System for Radio-Over-Fiber Networks," *Journal of Lightwave Technology*, vol. 35, pp. 979–988, Feb 2017.

[20] D. Wake, N. G. Walker, and I. C. Smith, "Zero-bias edge-coupled InGaAs photodiodes in millimetre-wave radio-fibre systems," *Electronics Letters*, vol. 29, pp. 1879–1881, Oct 1993.

[21] K. Li, X. Xie, Q. Li, Y. Shen, M. E. Woodsen, Z. Yang, A. Beling, and J. C. Campbell, "High-Power Photodiode Integrated With Coplanar Patch Antenna for 60-GHz Applications," *IEEE Photonics Technology Letters*, vol. 27, pp. 650–653, March 2015.

[22] A. Hirata, H. Ishii, and T. Nagatsuma, "Design and characterization of a 120-GHz millimeter-wave antenna for integrated photonic transmitters," *IEEE Transactions on Microwave Theory and Techniques*, vol. 49, pp. 2157–2162, Nov 2001.

[23] S. Shi, J. Bai, R. Nelson, C. Schuetz, P. Yao, G. J. Schneider, Y. Zhang, and D. W. Prather, "Ultrawideband Optically Fed Tightly Coupled Phased Array," *Journal of Lightwave Technology*, vol. 33, pp. 4781–4790, Dec 2015.

[24] D. D. Ross, M. R. Konkol, S. Shi, and D. W. Prather, "Photodiode-integrated UWB phased array antennas," in *2017 IEEE Photonics Conference (IPC)*, pp. 109–110, Oct 2017.

[25] M. R. Konkol, V. A. Carey, S. Shi, C. A. Schuetz, and D. W. Prather, "Millimeter-wave photonic tightly coupled array for 5G applications," in *2017 IEEE Avionics and Vehicle Fiber-Optics and Photonics Conference (AVFOP)*, pp. 43–44, Nov 2017.

[26] M. R. Konkol, D. D. Ross, S. Shi, C. E. Harrity, A. A. Wright, C. A. Schuetz, and D. W. Prather, "Photonic Tightly Coupled Array," *IEEE Transactions on Microwave Theory and Techniques*, vol. PP, no. 99, pp. 1–9, 2018.

[27] M. R. Konkol, D. D. Ross, S. Shi, C. E. Harrity, A. A. Wright, C. A. Schuetz, and D. W. Prather, "High-Power Photodiode-Integrated-Connected Array Antenna," *Journal of Lightwave Technology*, vol. 35, pp. 2010–2016, May 2017.

[28] D. D. Ross, M. R. Konkol, S. Shi, C. E. Harrity, A. A. Wright, C. A. Schuetz, and D. W. Prather, "Low-Profile High-Power Optically Addressed Phased Array Antenna," *Journal of Lightwave Technology*, vol. 35, pp. 3894–3900, Sept 2017.

[29] D. D. Ross, M. R. Konkol, S. Shi, and D. W. Prather, "Optically addressed ultra-wideband connected array antenna," in *2016 International Workshop on Antenna Technology (iWAT)*, pp. 207–210, Feb 2016.

[30] D. D. Ross, M. R. Konkol, C. Harrity, S. Shi, P. Yao, C. A. Schuetz, and D. W. Prather, "Integrated photodiode feeds for conformal UWB phased array antenna," in *2016 IEEE International Topical Meeting on Microwave Photonics (MWP)*, pp. 215–216, Oct 2016.

[31] M. R. Konkol, D. D. Ross, K. P. Shreve, C. E. Harrity, S. Shi, C. A. Schuetz, and D. W. Prather, "High-Power, Aperture Coupled Photonic Antenna," *IEEE Photonics Technology Letters*, vol. 29, pp. 1207–1210, July 2017.

[32] S. Shi, J. Bai, G. J. Schneider, Y. Zhang, R. Nelson, J. Wilson, C. Schuetz, D. W. Grund, and D. W. Prather, "Conformal Wideband Optically Addressed Transmitting Phased Array With Photonic Receiver," *Journal of Lightwave Technology*, vol. 32, pp. 3468–3477, Oct 2014.

[33] H. Bode, *Network Analysis and Feedback Amplifier Design*. Bell Telephone Laboratories series, Van Nostrand, 1945.

Copyright (c) 2018 IEEE. Personal use is permitted. For any other purposes, permission must be obtained from the IEEE by emailing pubs-permissions@ieee.org.

This is the author's version of an article that has been published in this journal. Changes were made to this version by the publisher prior to publication.
The final version of record is available at http://dx.doi.org/10.1109/JLT.2018.2834153

[34] R. Fano, "Theoretical limitations on the broadband matching of arbitrary impedances," *Journal of the Franklin Institute*, vol. 249, no. 1, pp. 57 – 83, 1950.

[35] G. Matthaei, L. Young, and E. Jones, *Microwave filters, impedance-matching networks, and coupling structures*. Artech House Microwave Library, McGraw-Hill, 1964.

[36] C. L. Goldsmith and B. Kanack, "Broadband microwave matching of high speed photodiodes," in *1993 IEEE MTT-S International Microwave Symposium Digest*, pp. 233–236 vol.1, June 1993.

[37] L. Breyne, G. Torfs, X. Yin, P. Demeester, and J. Bauwelinck, "Comparison between Analog Radio-over-Fiber and Sigma Delta Modulated Radio-over-Fiber," *IEEE Photonics Technology Letters*, vol. 29, pp. 1808–1811, Nov 2017.

[38] M. E. Godinez, C. S. McDermitt, A. S. Hastings, M. G. Parent, and F. Bucholtz, "RF Characterization of Zero-Biased Photodiodes," *Journal of Lightwave Technology*, vol. 26, pp. 3829–3834, Dec 2008.

[39] D. Pozar, *Microwave Engineering*. Wiley, 2004.

[40] J. Galejs, "Admittance of a rectangular slot which is backed by a rectangular cavity," *IEEE Transactions on Antennas and Propagation*, vol. 11, pp. 119–126, Mar 1963.

[41] G. Q. Luo, T. Y. Wang, and X. H. Zhang, "Review of Low Profile Substrate Integrated Waveguide Cavity Backed Antennas," *International Journal of Antennas and Propagation*, vol. 2013, p. 7.

[42] G. A. E. Vandenbosch and A. R. Van de Capelle, "Study of the capacitively fed microstrip antenna element," *IEEE Transactions on Antennas and Propagation*, vol. 42, pp. 1648–1652, Dec 1994.

[43] R. Levy, "Explicit formulas for Chebyshev impedance-matching networks, filters and interstages," *Proceedings of the Institution of Electrical Engineers*, vol. 111, pp. 1099–1106, June 1964.

[44] F. Giannini, R. Sorrentino, and J. Vrba, "Planar Circuit Analysis of Microstrip Radial Stub," in *1984 IEEE MTT-S International Microwave Symposium Digest*, pp. 124–125, May 1984.

[45] S. Mathew, T. Welker, N. Gutzeit, S. Spira, R. Stephan, J. Mller, and M. A. Hein, "Modulation characteristics of a laser-diode hybrid-integrated into a ceramic multilayer module for radio-over-fiber applications," in *2017 47th European Microwave Conference (EuMC)*, pp. 624–627, Oct 2017.

[46] J. Tatum, D. Smith, J. Guenter, and R. Johnson, "High-speed characteristics of VCSELs," in *Proc. SPIE*, vol. 3004, pp. 151–159, 1997.

[47] C. Balanis, *Antenna Theory: Analysis and Design*. Wiley, 2015.

[48] C. Jin, R. Li, A. Alphones, and X. Bao, "Quarter-Mode Substrate Integrated Waveguide and Its Application to Antennas Design," *IEEE Transactions on Antennas and Propagation*, vol. 61, pp. 2921–2928, June 2013.

[49] T. Chi, S. Li, J. S. Park, and H. Wang, "A Multifeed Antenna for High-Efficiency On-Antenna Power Combining," *IEEE Transactions on Antennas and Propagation*, vol. 65, pp. 6937–6951, Dec 2017.

Copyright (c) 2018 IEEE. Personal use is permitted. For any other purposes, permission must be obtained from the IEEE by emailing pubs-permissions@ieee.org.